

Article

# Towards GW-Scale Isolated Attosecond Pulse Far beyond Carbon K-Edge Driven by Mid-Infrared Waveform Synthesizer

Yuxi Fu <sup>1</sup> , Hua Yuan <sup>2</sup>, Katsumi Midorikawa <sup>1</sup>, Pengfei Lan <sup>2</sup> and Eiji J. Takahashi <sup>1,\*</sup>

<sup>1</sup> Attosecond Science Research Team, Extreme Photonics Research Group, RIKEN Center for Advanced Photonics, RIKEN, 2-1 Hirosawa, Wako, Saitama 351-0198, Japan; yxfu@riken.jp (Y.F.); kmidori@riken.jp (K.M.)

<sup>2</sup> School of Physics and Wuhan National Laboratory for Optoelectronics, Huazhong University of Science and Technology, Wuhan 430074, China; d201577059@hust.edu.cn (H.Y.); pengfeilan@hust.edu.cn (P.L.)

\* Correspondence: ejtak@riken.jp

Received: 8 November 2018; Accepted: 28 November 2018; Published: 1 December 2018



**Abstract:** We discuss the efficient generation of intense “water window” (0.28–0.54 keV) isolated attosecond pulses (IAPs) using a mid-infrared (MIR) waveform synthesizer. Our numerical simulations clearly indicate that not only a longer-wavelength driving laser but also a weak control pulse in the waveform synthesizer helps extend the continuum cutoff region and reduce the temporal chirp of IAPs in high-order harmonic generation (HHG). This insight indicates that a single-cycle laser field is not an optimum waveform for generating the shortest IAP from the viewpoints of reducing the attochirp and increasing the efficiency of HHG. By combining a waveform synthesizer technology and a 100 mJ MIR femtosecond pulse based on a dual-chirped optical parametric amplification (DC-OPA) method, a gigawatt-scale IAP (55 as with 10 nJ order) in the water window region can be generated even without attochirp compensation. The MIR waveform synthesizer is highly beneficial for generating a shorter IAP duration in the soft X-ray region because there are no suitable transparent dispersive materials that can be used for compressing the attochirp.

**Keywords:** synthesizer; attosecond; soft X-ray; high-order harmonic generation; infrared; high-energy

## 1. Introduction

Isolated attosecond pulses (IAPs) via high-order harmonic generation (HHG) have opened up a new branch of ultrafast science called attosecond physics [1]. In the past two decades, great advances have been made in attosecond physics, including the generation of IAPs with even shorter duration [2,3] and the real-time observation of electronic dynamics in atoms, molecules, and solids (see, for example, [4–7]). The first IAP source was demonstrated in the extreme ultraviolet (XUV) region (10–124 eV) using a few-cycle Ti:sapphire laser system ( $\lambda = 0.8 \mu\text{m}$ ) [8]. IAPs have been utilized with absorption spectroscopy to trace the ultrafast electron/ion dynamics in atoms and molecules. However, the efficient generation of IAPs driven by a Ti:sapphire laser has been limited to the XUV region. This is mainly due to the phase mismatch induced by free electrons from plasma because a high intensity greater than the ionization threshold of the medium is required for the generation of soft X-ray harmonics by a 0.8  $\mu\text{m}$  Ti:sapphire driving laser [9]. To extend the cutoff energy of HHG up to the water window region [2,10–13], Takahashi and co-workers proposed and demonstrated the use of a mid-infrared (MIR) laser for HHG in 2008 [14,15]. In contrast to the commonly used Ti:sapphire laser in the near-infrared region, the longer-wavelength MIR driving laser enables the HHG in the soft X-ray region with a neutral gas medium [14]. Then, the phase-matching technique [16–20] can be employed and the output HHG yield in the soft X-ray region can be significantly improved by the energy-scaling

method [21,22]. In addition, a longer-wavelength laser is advantageous for reducing the atto-chirp of IAPs, which is given as  $\propto \lambda^{-1}$  [23]. On the basis of these advantages, the wavelengths of driver lasers for generating IAPs have been shifting towards MIR wavelengths region [24]. In recent years, most HHG experiments with the aim of generating shorter IAPs in the soft X-ray region have employed few-cycle MIR laser pulses [2,3,12,13]. Indeed, the IAP duration has reached  $43 \pm 1$  as around the XUV region [3] and 53 as in the soft X-ray region [2].

However, IAPs generated using an MIR pulse face two principle problems even though the pulse duration was reached sub-50 as; one is the need for a method to compensate for attochirp, and the other is the reduced conversion efficiency due to the longer driver wavelength [25]. To compensate for the attochirp of HHG, a metal filter is generally employed [26]. We show the transmission and group delay dispersion (GDD) of different types of filters with a thickness of 1000 Å in Figure 1. From Figure 1b, it is clear that these metal filters are not helpful for compensating the attochirp of IAPs owing to the low GDD values in the soft X-ray region. Moreover, it is difficult to use a thick filter to increase the GDD owing to the low transmissivity. Even though super broadband continuum soft X-ray harmonics that supports an IAP with a sub-10-as transform-limited (TL) duration can be generated by a single-cycle MIR laser; unfortunately, the actual IAP duration increases to over few-tens-as owing to the attochirp. Therefore, the reduction of the attochirp is extremely important to create an IAP with short duration. In addition, the lower conversion efficiency for a longer laser wavelength is a serious problem for generating an intense soft X-ray IAP. It has been demonstrated that the HHG efficiency is scaled as  $\lambda^{-5}$ – $\lambda^{-6}$  with the driving laser wavelength  $\lambda$  [25,27]. Thus, the HHG yield is low usually in the soft X-ray region, and the applications of soft X-ray IAPs have been generally demonstrated by an IR/soft-X-ray cross-correlation method or single photon absorption process. It is clear that the development of a high-energy MIR laser with a few-cycle duration is of paramount importance for creating an intense soft X-ray IAP. Currently, numerous efforts have been devoted to develop a carrier envelope phase (CEP)-stabilized MIR laser with a few-cycle duration from an optical parametric amplifier (OPA) [28–30].

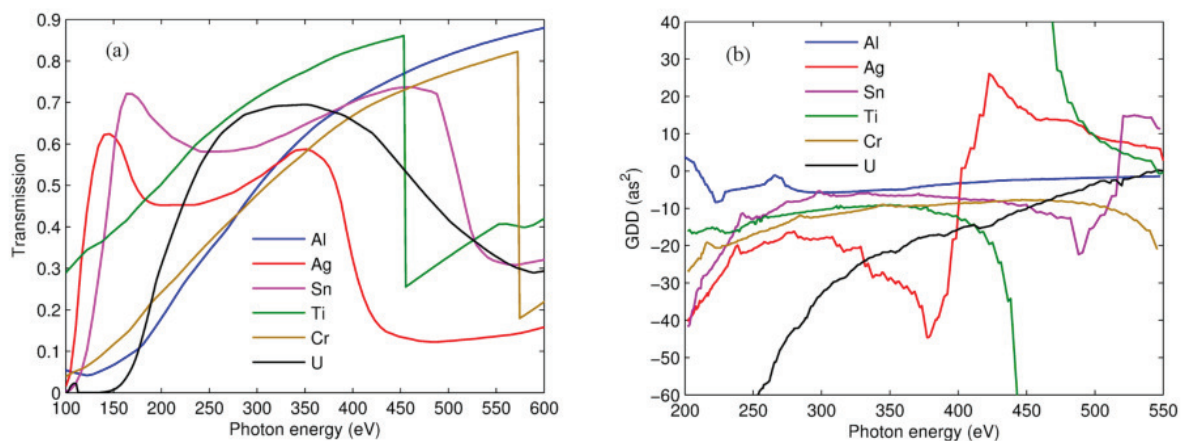


**Figure 1.** Transmission (a) and GDD (b) of various filters with thickness of 1000 Å. The transmission and GDD values are adopted and calculated based on the data obtained from [31].

To tackle the problem of the soft X-ray IAPs with low photon flux which is driven by a MIR pulse, in this work, we discuss and numerically demonstrate the efficient generation of intense soft X-ray IAPs using an MIR waveform synthesizer [32]. This demonstration realizes not only efficient cutoff-energy extension of the HHG, but also a reduction of the atto-chirp of IAPs. Our scheme is based on the idea of sub-cycle waveform shaping by synthesizing coherent multicycle MIR pulses with different wavelengths [33–36]. With the development of recent laser techniques, it has become possible to precisely synthesize and control the output of multicolor coherent light sources from different laser systems, such as fiber lasers [37] and OPA [38] and optical parametric chirp pulse

amplifier (OPCPA) [39] systems. Indeed, a fully stabilized terawatt (TW)-scale multicolor waveform synthesizer has been demonstrated by combining a Ti:sapphire laser and OPA [40]. By synthesizing a near-IR waveform, an IAP with 2.6 GW peak power was demonstrated in the XUV region [34,36].

In this paper, we simulate IAP generation using an MIR waveform synthesizer. In a classical calculation considering a single atom, we confirm that a longer wavelength not only helps extend the cutoff energy of HHG, but also reduces the attochirp. By mixing weak control pulses to synthesize the waveform, the cutoff can be further extended and the atto-chirp can be further reduced compared with that for a single-color pump. This result indicates that a single-cycle laser field is not an optimum waveform for generating the shortest IAP from the viewpoint of reducing the attochirp. In addition, the conversion efficiency of HHG can be increased by manipulating a waveform using a weak supplementary field. Our numerical simulations considering the propagation effect suggest that an IAP with a duration of  $\sim 55$  as can be obtained in the water window region even without atto-chirp compensation. Taking previous experimental results into account [14], therefore, we can expect to generate a GW-scale water window IAP with a pulse energy of 10 nJ order by using a 100 mJ MIR pump energy. On the basis of our simulation parameters, we present a designed experimental setup with information on how to achieve a fully stabilized TW-scale 100 mJ MIR waveform synthesizer based on a dual-chirped optical parametric amplification (DC-OPA) system.

The content of this paper is organized as follows: in Section 2, we first describe the advantages of an MIR waveform synthesizer. Then, we perform numerical simulation of a water window IAP driven by an MIR waveform synthesizer. In Section 3, a design for a water window IAP light source driven by a TW-scale MIR waveform synthesizer is presented. Finally, we summarize the results and present future prospects in Section 4.

## 2. Results and Discussion

### 2.1. Advantages of an MIR Waveform Synthesizer for Generating an Isolated Attosecond Pulse

The mechanism of HHG can be understood through the behaviour of an electron inside a strong laser field using a three-step model [41], which involves tunnel ionization of the electron, acceleration by the laser field, and a return to the parent ion with the release of the gained energy in the form of a photon. Thus, following the three-step model, it is very helpful to analyze the attosecond pulse generation in HHG by calculating the return kinetic energy (RKE) of electrons after ionization in a classical manner. Then, the energy of the emitted photons in HHG can be calculated as the sum of RKE and the ionization potential of the atom or molecules. In this classical calculation, an Ne atom is selected, which has an ionization potential of 21.56 eV. As a simple example, we perform the calculation using a single-cycle (FWHM) laser pulse. The electric field with a CEP of 0 and a Gaussian pulse envelope is shown in Figure 2a. Figure 2b shows the calculation results for driving laser wavelengths of  $\lambda$  and  $2\lambda$  with the same intensity. Peak A and Peak B represent different cutoff energies when electrons are ionized near each electric field peak in adjacent half cycles, which are indicated by  $t_a$  and  $t_b$  in Figure 2a, respectively. The short and long trajectories result from different ionization times in the same half cycle of the electric field peak. In an experiment, only one trajectory can be selected by placing the gas medium before (long trajectory) or after (short trajectory) the laser focus. Thus, a supercontinuum bandwidth, which determines the shortest attainable attosecond pulse duration under a TL condition, is determined by the difference between the cutoff energies of Peak A and Peak B. It is clear that the laser field with  $2\lambda$  wavelength not only markedly increases the cutoff energy ( $E_{\text{cutoff}} = I_p + 3.17 U_p$ , where  $U_p \propto \lambda^2$  and  $I_p$  is the ionization potential) but also significantly extends supercontinuum bandwidth, which is approximately four times ( $\propto \lambda^2$ ) that for the laser field at the wavelength of  $\lambda$ . Hence, a longer driving laser wavelength is very helpful for obtaining a broader supercontinuum spectrum with higher photon energy, which is further proved by the calculated photon energy under different emission times (group delay (GD)) in Figure 2c under different driving wavelengths. To examine the temporal chirp (called the attochirp) of the photons in Figure 2c under

the same laser intensity but with different wavelengths, the GDD is calculated and shown in Figure 2d. Short and long trajectories are positively and negatively chirped, respectively. The photon energies with minimum chirps (minimum GDD values for short or long trajectories) are the photons with approximately half of the cutoff energy, which are located in the plateau regions of high harmonics (HH) spectra. Comparing the GDD values at the same photon energies below the cutoff region (plateau region), short trajectories with less atto-chirp are obtained for shorter driving wavelengths. However, the most important feature is that a longer driving laser wavelength not only markedly increases the cutoff energy, but also significantly reduces attochirp at higher photon energies. It should be noted that, by increasing laser intensity for a shorter wavelength driving laser, the cutoff energy can also be extended with reduced attochirp. However, the significantly increased ionization ruins phase matching between driving laser and HHs, which generally should be avoided in HHG.

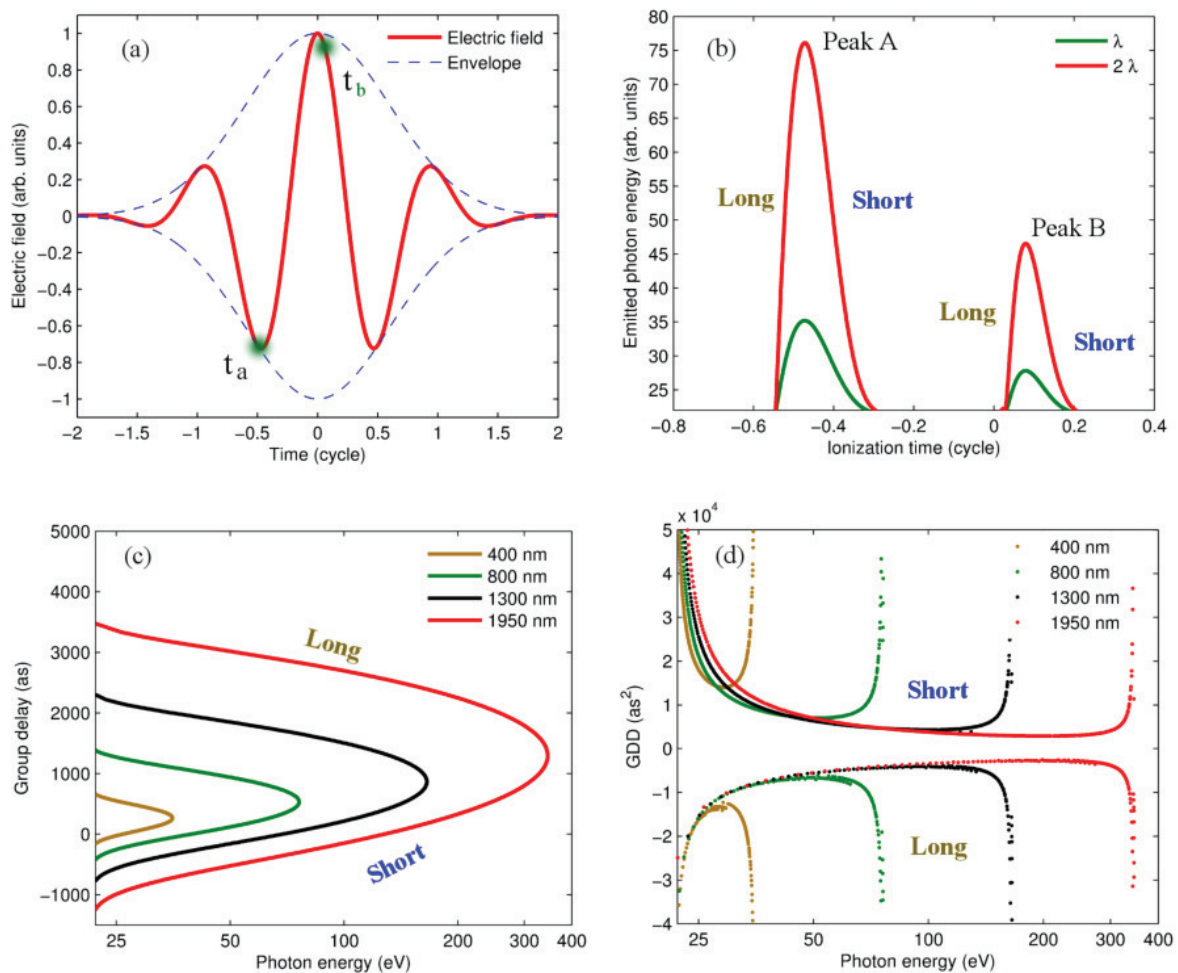


**Figure 2.** (a) electric field of a single cycle pulse; (b) classical calculation of photon energies with two cutoffs occurring in two subsequent half cycles of electric field, for driving laser wavelengths of  $\lambda$  and  $2\lambda$ ; (c) classical calculation of photon energies under different wavelengths as a function of recollision time (group delay); (d) GDD values calculated from (c).

Moreover, mixing a weak control pulse, i.e., synthesizing a waveform, is very helpful for reducing attochirp [42,43]. The synthesized field in this paper is expressed as

$$E f_s = \sum_{i=1}^N E_i e^{-2 \ln 2 ((t - \Delta t_i) / \tau_i)^2} \cos(\omega_i (t - \Delta t_i) + \phi_i), \quad (1)$$

where the subscript denotes the field with  $i = 1$  indicating the main driving pulse,  $E$  denotes the amplitude of the electric field,  $\tau$  denotes the pulse duration (FWHM),  $\Delta t$  denotes the delay,  $\omega$  denotes the angular frequency, and  $\phi$  denotes the CEP. First, we employ a single-color pulse at  $1.95 \mu\text{m}$  with a single-cycle pulse duration, an intensity of  $2.9 \times 10^{14} \text{ W/cm}^2$ , and a CEP of  $-\pi$ , which we call “one color 1” (see Figure 3). The electric field ( $E_{f_1}$ ) is plotted as a black curve in Figure 3a. The GD and GDD of the generated photons are given by black curves in Figure 3b,c, respectively. The cutoff energy is 350 eV. The minimum absolute GDD (larger values indicate larger atto-chirp) in the plateau region is  $\sim 3000 \text{ as}^2$  for both short and long trajectories. By mixing a weak control pulse at  $1.356 \mu\text{m}$  with an intensity of  $5 \times 10^{13} \text{ W/cm}^2$  (17% of that of the main driving laser) and the same pulse duration, a CEP of  $0.5\pi$ , and a delay of  $-1.13 \text{ fs}$  (quarter cycle of the control pulse), the electric field ( $E_{f_s}$ ) is modified as shown by the red curve in Figure 3a. Then, the cutoff energy is significantly increased by approximately 1.5-fold to 530 eV as shown by the red curve in Figure 3b. More importantly, the absolute GDD values are greatly reduced to  $\sim 1500 \text{ as}^2$ , which is approximately half that in the one-color case. For comparison, we also employ the same single-color pulse as that of  $E_{f_1}$  but with an increased laser intensity of  $4.44 \times 10^{14} \text{ W/cm}^2$  ( $E_{f_2}$ ), for which the electric field waveform is shown by the blue curve (labelled by “one color 2”) in Figure 3a. The cutoff energy, as shown by the blue curve in Figure 3b, is 530 eV, which is the same as that of the two-color field ( $E_{f_s}$ ). However, the temporal window of the emission (see the group delay) is larger than that for the two-color field, indicating that the attochirp is also larger. The minimum absolute GDD is  $\sim 1850 \text{ as}^2$ , which is much less than that for the single-color field ( $E_{f_1}$ ) with a lower intensity, but still larger than that for the two-color synthesized field ( $E_{f_s}$ ). At the cutoff region, the GDD is even larger. Thus, a weak field employed in a waveform synthesizer helps to reduce the attochirp compared with that for a single-color field, making it helpful for generating short IAPs without chirp compensation. For example, for a TL duration of 50 as (FWHM) at 280 eV (cutoff region) generated by a single-color field  $E_{f_1}$ , the actual duration of the IAP is  $\sim 200$  as owing to the attochirp. In the two-color synthesized field  $E_{f_s}$ , the actual IAP duration is 120 as at 450 eV (cutoff region), for which the pulse duration is significantly reduced. In the single-color field  $E_{f_2}$ , the actual IAP duration is 150 as at 450 eV (cutoff region), which is also longer than that for the two-color synthesized field. In fact, by constructing an optimum waveform using a synthesizer, it is possible to obtain IAPs without any attochirp [44]. Moreover, using the above electric fields, we calculate the HHG spectrum of a single Ne atom using the Lewenstein model [45] as shown in Figure 4. The Ne medium is kept neutral with the ionization ratio maintained at less than 1% for all the laser fields. The spectral modulation is due to interference between short and long trajectories, where the trajectory can be selected by placing the medium after or before the laser focus [46]. Comparing the HHs generated by the electric field  $E_{f_s}$  with  $E_{f_1}$  (one color 1), the cutoff is markedly extended. For HHs with the same photon energies (below 350 eV), the conversion efficiency (from the driving laser to the HHs) is one order higher. Compared with the HH generated by the field  $E_{f_2}$  (one color 2), which generates the same cutoff as the two-color synthesizer, the conversion efficiency is  $\sim 2.5$  times higher for  $E_{f_s}$ , which is due to the higher instantaneous ionization rate caused by the increased electric field near  $-2.6 \text{ fs}$  for  $E_{f_s}$ . From these results, it is clear that a single-cycle laser field is not an optimum waveform for IAP generation from the viewpoints of reducing the attochirp and increasing the conversion efficiency. In contrast, a waveform synthesizer is helpful for efficiently generating shorter IAPs by decreasing the attochirp.

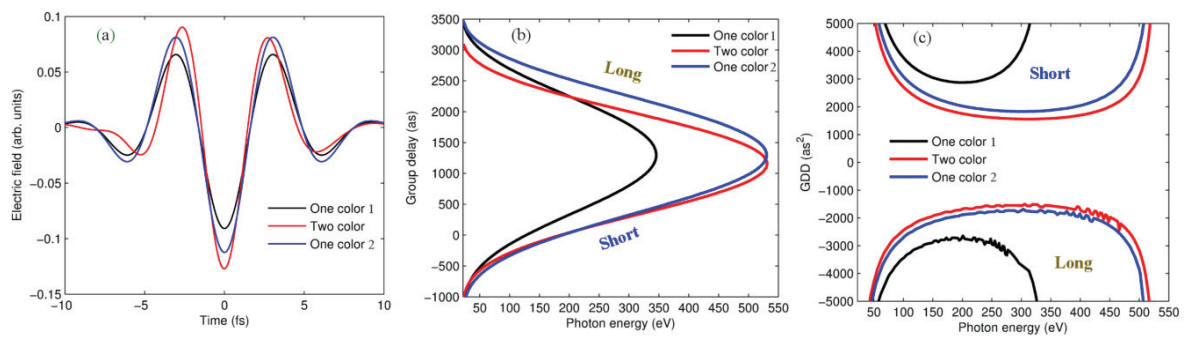


**Figure 3.** Reducing attochirp using a waveform synthesizer. (a) Electric field of a single-color 1.95  $\mu\text{m}$  pulse (single cycle,  $\text{CEP} = -\pi$ ) with intensities of  $2.9 \times 10^{14} \text{ W/cm}^2$  (black,  $E_{f1}$ ) and  $4.44 \times 10^{14} \text{ W/cm}^2$  (blue,  $E_{f2}$ ) and a two-color (red,  $E_{f3}$ ) synthesizer (Intensities are  $2.9 \times 10^{14} \text{ W/cm}^2$  at 1.95  $\mu\text{m}$  and  $5 \times 10^{13} \text{ W/cm}^2$  at 1.356  $\mu\text{m}$ ); (b) photon energies under each group delay (emission time); (c) GDD values calculated from (b).

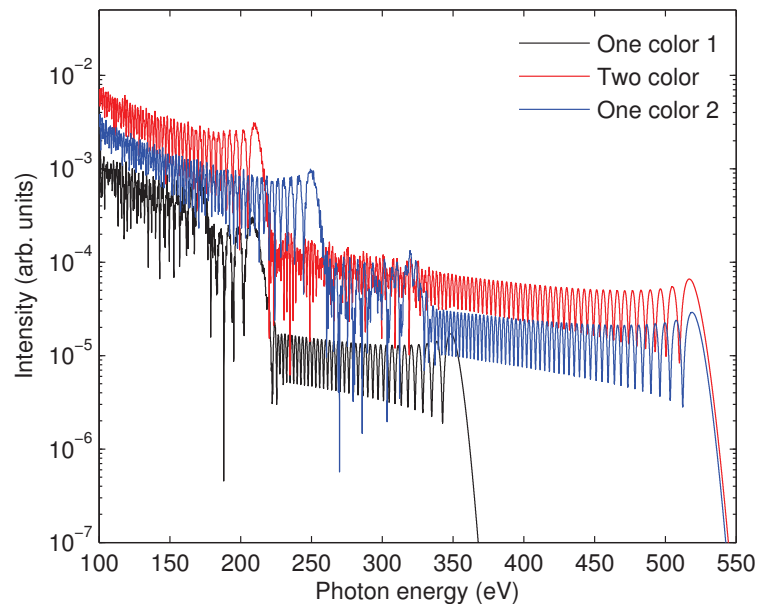


**Figure 4.** HHs spectra calculated for a single atom for each electric field in Figure 3a.

## 2.2. Generation of Water Window IAPs from an MIR Waveform Synthesizer

For IAP generation by a single-color pump, a driving laser with a few-cycle duration is generally required. In contrast, a driving laser with much longer duration (multicycle) can be employed to generate a significantly stronger IAP in a waveform synthesizer [33–36], where the central peak of the pulse envelope is close to that of a subcycle pulse but with a modified/optimized electric field waveform. In this section, we simulate the generation of IAPs in the water window region using a multicycle MIR waveform synthesizer in a gas cell.

### 2.2.1. Simulation Method

The HHG in an atomic gases can be theoretically described by the response of a single atom and the collective response of the macroscopic gas to the laser and harmonic fields. In our calculation, we apply the strong-field approximation model (SFA) [45] to calculate the harmonic radiation. The time-dependent dipole momentum is [45]

$$d_{nl}(t) = i \int_{-\infty}^t dt' \left[ \frac{\pi}{\varepsilon + i(t-t')/2} \right]^{3/2} \times d_{\text{rec}} [p_{\text{st}}(t', t) + A(t)] d_{\text{ion}} [p_{\text{st}}(t', t) + A(t')] \times \exp [-iS_{\text{st}}(t', t)] E(t')g(t') + c.c., \quad (2)$$

where  $E(t)$  is the driving laser field,  $A(t)$  is the vector potential, and  $\varepsilon$  is a positive regularization constant.  $d_{\text{rec}}$  and  $d_{\text{ion}}$  are the recombination and ionization matrix elements, respectively.  $p_{\text{st}}$  and  $S_{\text{st}}$  are the stationary momentum and quasiclassical action, respectively.  $g(t)$  represents the ground-state amplitude, which is calculated by the Ammosov–Delone–Krainov (ADK) tunneling model [47]. Then, the harmonic spectrum is obtained as the Fourier transform of the time-dependent dipole acceleration  $a(t)$ ,

$$a_q = \frac{1}{T} \int_0^T a(t) \exp(-iq\omega t), \quad (3)$$

where  $a(t) = \ddot{d}_{nl}(t)$ , and  $T$  and  $\omega$  are the duration and frequency of the driving pulse, respectively.  $q$  is the harmonic order.

To simulate the collective response of the macroscopic gas, we separately numerically solve the Maxwell wave equations for the fields of the laser pulse  $E_l$  and the harmonics  $E_h$  in a cylindrical coordinate,

$$\nabla^2 E_l(r, z, t) - \frac{1}{c^2} \frac{\partial^2 E_l(r, z, t)}{\partial t^2} = \frac{\omega_p^2(r, z, t)}{c^2} E_l(r, z, t), \quad (4)$$

$$\nabla^2 E_h(r, z, t) - \frac{1}{c^2} \frac{\partial^2 E_h(r, z, t)}{\partial t^2} = \frac{\omega_p^2(r, z, t)}{c^2} E_h(r, z, t) + \mu_0 \frac{\partial^2 P_{nl}(r, z, t)}{\partial t^2}, \quad (5)$$

where  $\omega_p = [4\pi n_e(r, z, t)]^{1/2}$  is the plasma frequency,  $P_{nl}(r, z, t) = [n_0 - n_e(r, z, t)]d_{nl}(r, z, t)$  is the nonlinear polarization of the medium,  $n_0$  is the gas density, and  $n_e(t) = n_0 \left[ 1 - \exp \left( - \int_{-\infty}^t w(t') dt' \right) \right]$  is the free-electron density in the gas, where  $w(t)$  is the electron ionization rate. The equations here take into account both temporal plasma-induced phase modulation and the spatial plasma-lensing effects on the driving field. Equations (4) and (5) can be numerically solved by the Crank–Nicholson method as described in Refs. [48,49]. Finally, the high harmonics at the exit of the gas medium are multiplied by the transmissivity of the gas [31].

### 2.2.2. Simulation Results

First, we employ a two-color waveform synthesizer, which contains a main driving pulse at 1.95  $\mu\text{m}$  and a control pulse at 1.35  $\mu\text{m}$ . Their intensities are  $2.9 \times 10^{14} \text{ W/cm}^2$  and  $5 \times 10^{13} \text{ W/cm}^2$ , respectively, and both have a pulse duration of 30 fs (FWHM). Their CEPs are  $-\pi$  and  $1.5\pi$ , respectively, and the time delay between the two pulses is 1.13 fs. Then, the intensity profile of the synthesized electric field is shown by the orange shaded curve in Figure 5a. The intensity ratio between the main peak and the second strongest side peak is similar to that of a 1.4-cycle laser at 1.7  $\mu\text{m}$  (green solid). Because HHG is very sensitive to the electric field strength, only the central electric field peak contributes to the harmonic continuum in the cutoff region. Thus, even though we employ multicycle laser pulses, the synthesized pulse is sufficient to generate supercontinuum HH spectra, that support IAPs. The generated HH spectrum under a 32 torr pressure in a 60-mm-long Ne gas cell is shown in Figure 5b, which is phase-matched near 320 eV. By increasing the Ne pressure to 101 torr in a 70-mm-long cell, the supercontinuum is phase-matched to higher photon energies near 532 eV, as shown in Figure 5c. Thus, we were able to generate HH supercontinua in the entire water window region, which covers the k-edges of carbon (284 eV) to oxygen (543 eV). To extract these supercontinua

from driving laser pulses from the viewpoint in an experiment, we employ a 1000-Å-thick Sn filter in the simulation. Then, we calculate the IAP envelope of the HH supercontinua with a 1000 Å Sn filter in Figure 5b. The result is shown in Figure 6a. An IAP with 63 as (FWHM) duration is obtained as shown by the red solid curve. The TL duration is 27 as (FWHM). In addition, we calculate the IAP of the supercontinuum in Figure 5c after a 1000-Å-thick Sn filter. Its pulse envelope with a duration of 66 as is shown in Figure 6b. The TL pulse is shown by the black curve and has a duration of 28 as. Note that the filters are not helpful for compensating the chirp of IAPs owing to the low GDD values, as discussed above.

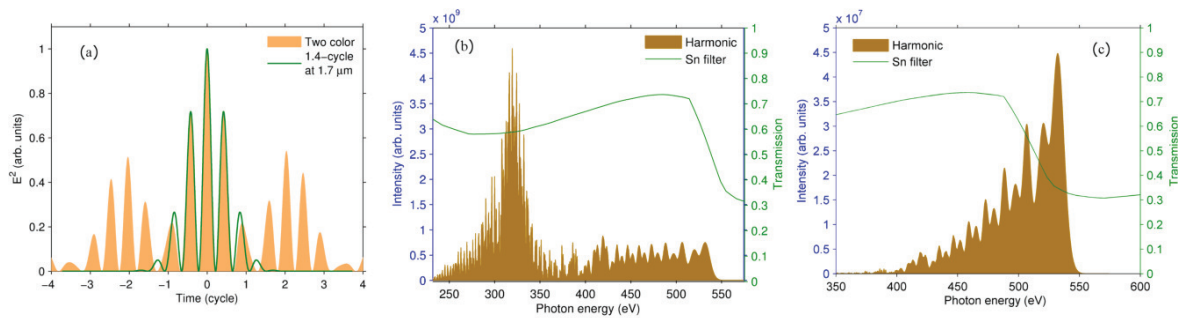


**Figure 5.** (a) intensity ( $E^2$ ) of electric fields of a two-color synthesizer (orange shaded) and a 1.4-cycle laser pulse at 1.7  $\mu\text{m}$  (green). HH spectra obtained using 60-mm-long (b) and 70-mm-long (c) gas cells. Transmission of Sn filters are plotted in (b,c).

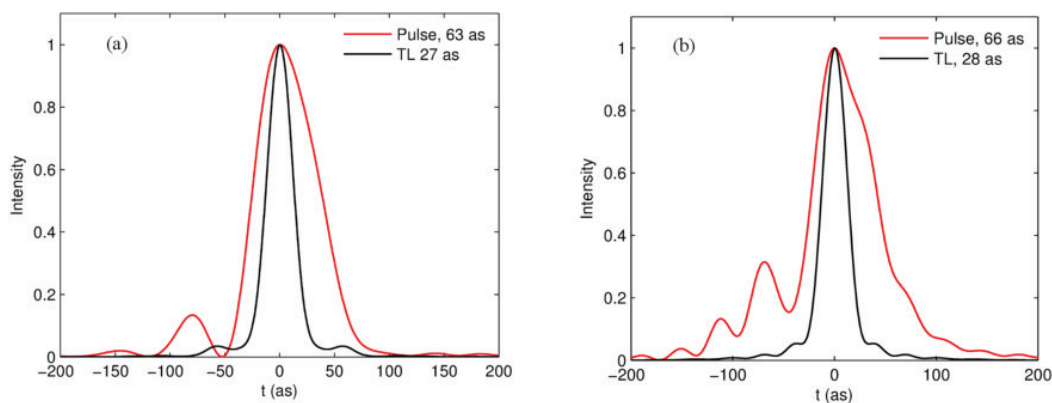


**Figure 6.** (a,b) show IAPs calculated by the spectra in Figure 5b,c, respectively, generated by the two-color synthesizer. Red curves indicate obtained IAP durations while black curves indicate TL durations.

Next, we add one more control pulse to the waveform synthesizer. The wavelengths of the main driving pulse and the first and second control pulses are 1.9  $\mu\text{m}$ , 1.38  $\mu\text{m}$ , and 0.8  $\mu\text{m}$ , respectively. The intensities are  $2.5 \times 10^{14}$  W/cm<sup>2</sup>,  $5 \times 10^{13}$  W/cm<sup>2</sup>, and  $5 \times 10^{12}$  W/cm<sup>2</sup>, respectively, with a pulse duration of 30 fs (FWHM). The CEPs are  $-\pi$ ,  $1.5\pi$  and  $\pi$ , respectively. The delays of first and second pulses are 1.13 fs and 0 fs, respectively. The electric field of the synthesizer is shown in Figure 7a. It can be seen that, except for the central main peak, the electric field peaks are more suppressed than those for the two-color case. Thus, the effective waveform for HHG is further shortened, and is similar to a 0.99-cycle pulse at 1.73  $\mu\text{m}$  (green), in terms of the intensity ratio between the main and second-strongest side peaks. Employing the synthesized electric field to drive HHG, we simulate HH spectra in an Ne gas cell. When the pressure is 32 torr in the 60-mm-long cell, an HH continuum spectrum with a peak intensity at 350 eV is obtained, as shown in Figure 7b. By increasing the pressure to 101 torr in the 70-mm-long cell, the HH continuum spectrum is phase-matched to a higher photon energy near 480 eV, as shown in Figure 7c. The calculated IAP for the spectrum in Figure 7b after a 1000-Å-thick Sn filter is shown by the red curve in Figure 8a and has a pulse

duration of 55 as. The TL duration is 23 as, as shown by the black curve. A slightly longer IAP with a duration of 71 as is obtained for the spectrum in Figure 7c, as shown in Figure 8b by the red curve. Note that the attochirp limits the shortest pulse duration even though the broad supercontinuum supports a TL duration of 22 as, which is shorter than one atomic unit (24 as).

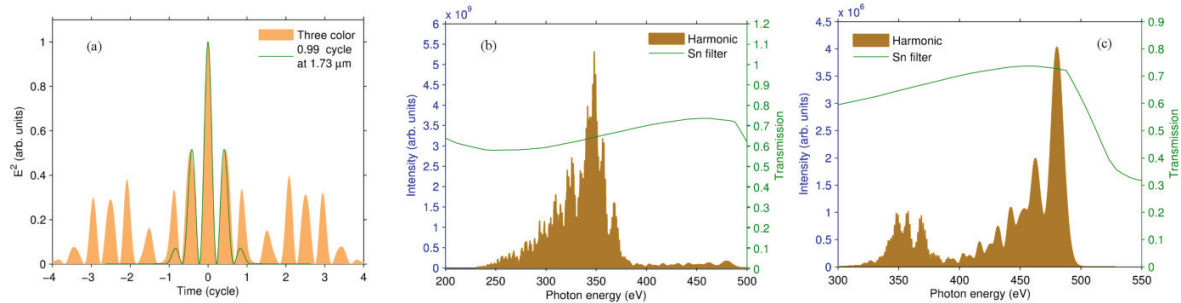


**Figure 7.** (a) intensity ( $E^2$ ) of electric fields of three-color synthesizer (orange shaded) and a 0.99-cycle laser pulse at  $1.73 \mu\text{m}$  (green). HH spectra after 60-mm-long (b) and 70-mm-long (c) gas cells. Transmission of Sn filters are plotted in (b,c).

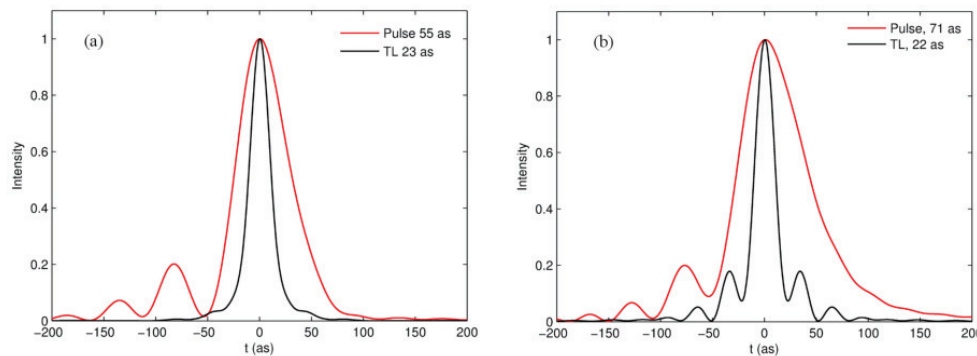


**Figure 8.** (a,b) show IAPs calculated from spectra in Figure 7b,c, respectively, generated by the three color synthesizer. Red curves indicate obtained IAP durations while black curves indicate TL durations.

### 3. Design for a TW-Scale MIR Waveform Synthesizer for Generating Water Window IAP

HHG experiments in the water window region have been demonstrated by many groups [2,12,50,51]. In 2008, we demonstrated the generation of a coherent water window X-ray by extending the plateau region of high-order harmonics under a neutral-medium condition [14,15]. The conversion efficiency of the HHG driven by a  $1.65 \mu\text{m}$  laser in Ne was approximately  $6.5 \times 10^{-8}$  at 300 eV. Considering our earlier experiment results, IAPs with pulse energy of 10 nJ order in the water window region can be expected by using a 100-mJ-class MIR waveform synthesizer as a driver laser. To perform the experiment, we design a TW-scale multicycle MIR waveform synthesizer with a 10 Hz repetition rate in accordance with the simulation results in Section 2.

#### 3.1. TW-Class MIR Laser Source Based on DC-OPA

In our recent work, we successfully generated an IR laser with 100-mJ-class energy, a TW-class peak power IR laser, and a 10 Hz repetition rate [52] using a DC-OPA [53–57]. The nonlinear crystals employed in the DC-OPA system were  $\beta\text{-BaB}_2\text{O}_4$  (BBO) crystals. Using this laser source, laser pulses with three colors, as shown in Figure 9, can be provided to construct a waveform synthesizer. The two colors of the IR pulses labelled main pulse and control pulse 1 in the synthesizer are flexibly tunable in the ranges of  $1.6\text{--}2.4 \mu\text{m}$  and  $1.2\text{--}1.6 \mu\text{m}$  (these two colors are generated in pairs, one is the same as the seed used for DC-OPA, the other is obtained from difference frequency generation (DFG)), respectively, which is very helpful for manipulating the waveform in the synthesizer by tuning the wavelength [33]. The third color, control pulse 2 is provided by a Ti:sapphire chirped pulse amplifier (CPA), which is

also a pump source for the DC-OPA system. The duration of the compressed pulse with a stabilized CEP is  $\sim 28$  fs (FWHM) [58]. However, the durations of the main pulse and control pulse 1 are 40–50 fs (FWHM), which are longer than those in our simulation in Section 2, which required a pulse duration of 30 fs (FWHM).

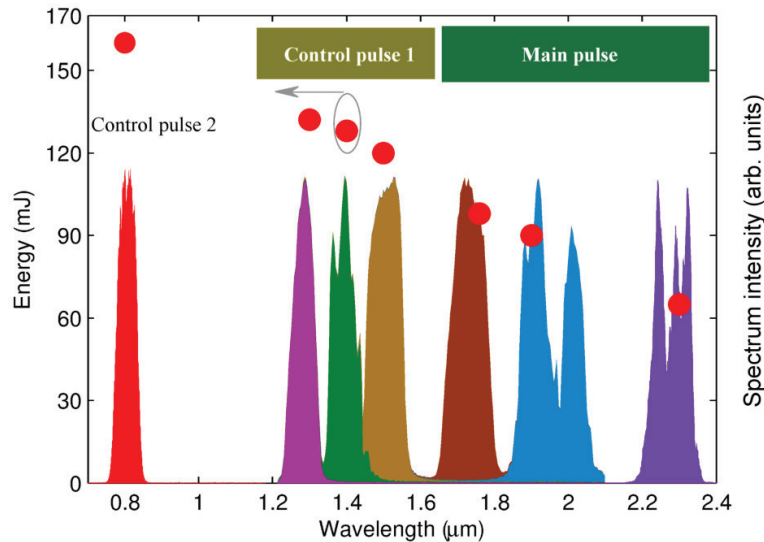


**Figure 9.** Hundred millijoule and multi-TW-class MIR fs pulses generated by a BBO-crystal-based DC-OPA system with flexible tunability in the range of 1.2–2.4  $\mu\text{m}$ . Main pulse and control pulse 1 are generated in pairs in the DC-OPA system through parametric amplification. The pulse energy and spectrum at each central wavelength are shown by red dots and shaded curves, respectively. The 0.8  $\mu\text{m}$  laser is from a CEP-stabilized Ti:sapphire laser system, which is also a pump source for DC-OPA.

We find that  $\text{BiB}_3\text{O}_6$  (BiBO) [59,60] and  $\text{LiB}_3\text{O}_5$  (LBO) crystals are suitable for generating TW-class IR pulses by a DC-OPA system with shorter durations (shorter than five optical cycles) near 1.95  $\mu\text{m}$  and 1.35  $\mu\text{m}$ . We calculate phase-matching results over a broad bandwidth which are shown in Figure 10a,b as two-dimensional plots for BiBO and LBO crystals with cutting angles of  $\theta = 11^\circ$  (XZ plane) and  $\phi = 15^\circ$  (XY plane), respectively. A smaller phase mismatch indicates better phase matching. For the BiBO crystal, the two designed phase-matching conditions (the designed signal chirp is the same as that of the seed) in experiment are plotted as blue and red curves. For the LBO crystal, the designed phase-matching condition (red) in the experiment follows the optimal phase-matching. Thus, we can use both BiBO and LBO crystals for the DC-OPA system to create IR pulses for the synthesizer. Because LBO has a much higher damage threshold as well as a very large aperture, it is the preferred crystal for our DC-OPA system. When we employ a LBO crystal with a 30 mm aperture, the durations of the pump and seed pulses are  $\sim 2$  ps. Moreover, in Figure 10, the chirp signs of the pump and seed are opposite under an optimized phase-matching condition. Hence, we can employ negative and positive chirps for the pump and seed pulses in the DC-OPA system, which are precisely controlled by changing the grating separation and using an acousto-optic programmable dispersive filter (AOPDF), respectively. Then, the DFG pulse is negatively chirped. With these chirp signs, we can compress the pulses using bulk materials after the DC-OPA (e.g., fused silica for the main pulse and SF10 for control pulses), which do not deteriorate the stability of CEPs.

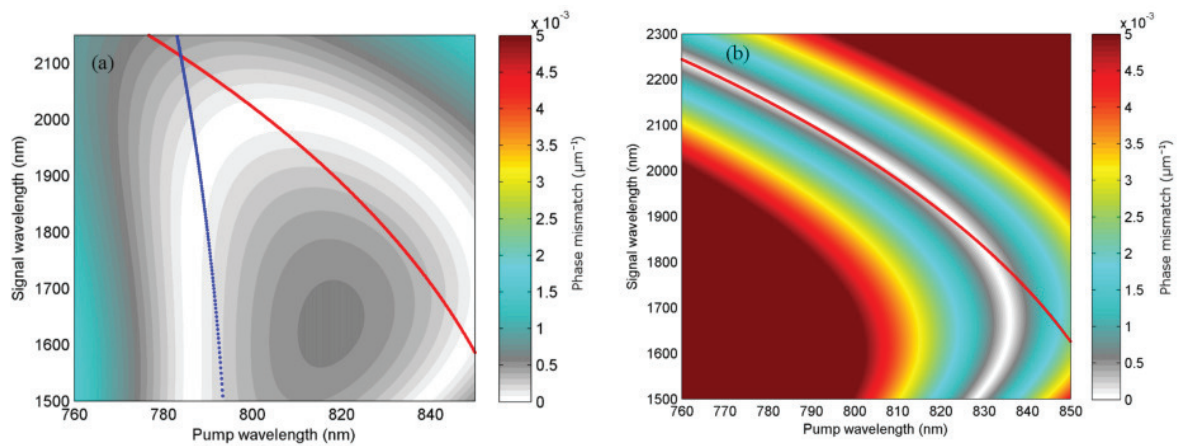


**Figure 10.** Calculated phase mismatch of a BiBO crystal (a) and an LBO crystal (b). The white region indicates almost perfect phase matching. The solid curves show designed chirps for IR pulses to achieve high conversion efficiency as well as a broad spectral bandwidth. For the BiBO crystal, the two cases of chirp designs for the seed pulse are shown by blue and red curves. The horizontal axis indicates the spectral range of the pump laser for the DC-OPA system.

On the basis of these considerations, we design the complete experimental setup shown in Figure 11, which mainly consists of four parts: a 10 Hz Ti:sapphire laser with  $\sim 700$  mJ energy and parts for the generation of a TW IR laser by DC-OPA, the stabilization of the CEP of the Ti:sapphire laser (thus stabilizing the CEPs of the main pulse, control pulse 1 and control pulse 2), and the stabilization of the relative timing jitter and phase jitter in three-color pulses.

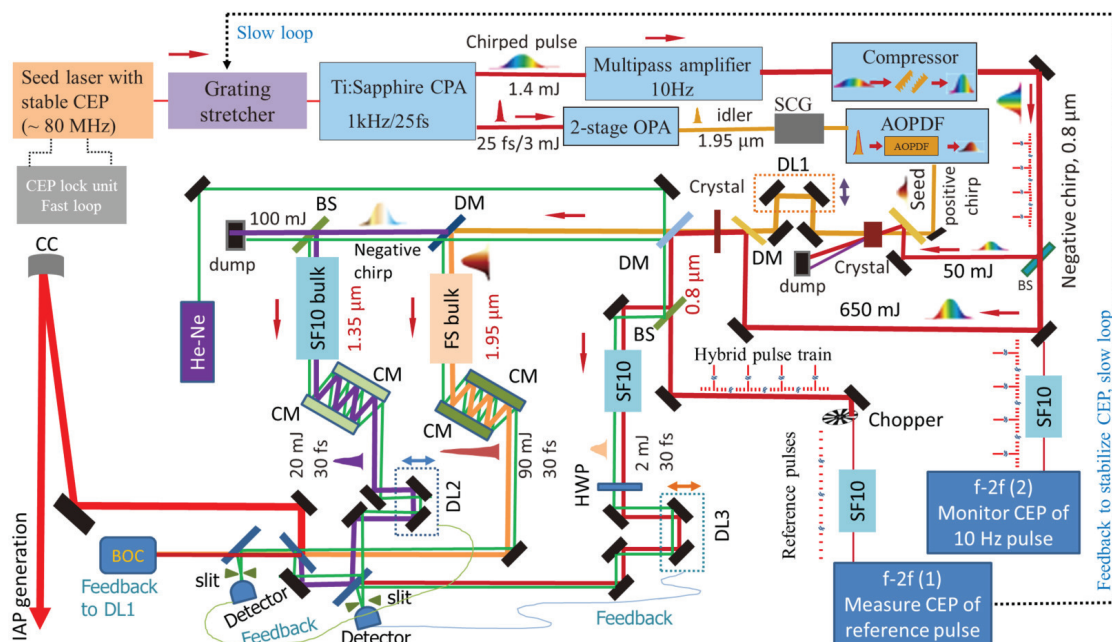


**Figure 11.** Schematic drawing of a TW-scale MIR waveform synthesizer for generating water window IAPs. CPA, chirped pulse amplifier; SCG, supercontinuum generation; DM, dichroic mirror; DL, delay line; BS, beam splitter; FS, fused silica; CM, chirp mirror; CC, concave mirror; BOC, balanced optical cross-correlator; HWP, half-wave plate.

### 3.2. Stabilizing the Delay Jitter and Phase Jitter in the Synthesizer

Temporal synchronization between each color inside a synthesizer strongly affects the waveform; thus, the temporal synchronization must be stabilized in order to maintain a stable waveform from

shot to shot [36]. As shown in Figure 11, the synchronization can be achieved in two steps [40]. First, by introducing a continuous wave (CW) laser (He-Ne) which passes through each beam path to form an interferometer, the timing jitter between each beam path can be monitored and minimized by introducing active feedback [36] to delay stages DL2 and DL3. Second, the timing jitter between the main pulse and control pulse 2 can be monitored by a balanced optical cross-correlator (BOC) [61,62], and thus can be minimized by introducing further active stabilization (feedback to DL1). Then, the temporal synchronization between each color of the synthesizer is stabilized. Moreover, another parameter that must be considered is the CEP stability. This is because the CEP shift results in shot-to-shot changes in the intensity of IAPs, and multiple bursts of IAPs appear at some CEP values [33]. Thus, to obtain a stable IAP for each laser shot, the CEP of each color must be stabilized. First, the seed pulse for the DC-OPA system at  $\sim 1.9 \mu\text{m}$  is generated through difference frequency generation in a standard OPA system (see Figure 11). Thus, the CEP of seed as well as its amplification after the DC-OPA system is passively stabilized. However, owing to timing jitter between the pump and the white-light-generated seed in the standard OPA, the CEP of the seed slightly fluctuates. Thus, feedback utilizing copropagating pump pulses is introduced to minimize the timing jitter (not shown in Figure 11). After the CEP of the seed pulse is stabilized, it is necessary to stabilize the CEP of the 10 Hz pump pulse for the DC-OPA system. In our previous experiment, we demonstrated the stabilization of the CEP of each shot of a TW laser with a 10 Hz repetition rate [58,63] using an indirect CEP stabilization method. In this setup, we employed the same method. Details are shown in Figure 11. A reference pulse ( $\sim 1 \text{ mJ}$ ) with a repetition rate of 990 shots/s copropagates with a high-energy ( $\sim 700 \text{ mJ}$ ) 10 Hz pulse to form a hybrid pulse train. Thus, these pulses experience exactly the same CEP noises, which are induced by grating vibration in the compressor, temperature changes, air turbulence, and beam-pointing fluctuation. Because the reference pulse energy is more than two orders lower than the high-energy 10 Hz pulse, it does not contribute to amplification in DC-OPA. After the two-stage DC-OPA, the hybrid pulse train is separated from the IR pulses. A small portion ( $\sim 2 \text{ mJ}$ ) of the 10 Hz pulse is compressed by an approximately 10-cm-long SF10 bulk (when the LBO crystal is employed in DC-OPA), and is utilized as control pulse 2 in the synthesizer. The main portion of the reference pulse is split into two beams, one beam is used for monitoring the CEP of high-energy 10 Hz pulses after compression by the SF10 bulk. The other beam, from which only the reference pulse is selected by an optical chopper, is utilized for monitoring CEP jitter (after compression by the SF10 bulk) at 500 Hz and as feedback to move the grating in the grating stretcher as a means of stabilizing the CEP. Since we utilize fused silica and SF10 bulks to compress the durations of the main pulse and control pulse 1, the CEPs are not deteriorated. Thus, the CEP of each color pulse is stabilized. After stabilizing both the timing jitter and phase jitter, our TW-class IR waveform synthesizer is fully stabilized and ready to generate IAPs through HHG. To obtain the same focus sizes of all the pulses in the waveform synthesizer for HHG, the focus sizes of the control pulses are adjusted to be the same as that of the main pulse by controlling their beam sizes.

#### 4. Conclusions

We discussed the generation of an intense water window IAP using an MIR waveform synthesizer. By synthesizing a three-color field in the MIR region, the intensity ratio between the central peak and the highest side peak was 0.5, which was almost the same as that of a single-cycle laser. Thus, a 100 mJ MIR three-color waveform synthesizer can generate a GW-scale peak power with a 10-nJ-order energy supercontinuum in the water window region from an Ne gas medium, which supports IAPs of  $\sim 50\text{--}70 \text{ as}$  (FWHM) duration according to our simulation, even without chirp compensation. The weak control pulses in the waveform synthesizer not only help to shorten the duration of the effective electric field, but also extend the cutoff and reduce the attochirp. Moreover, the waveform synthesizer helps to improve the conversion efficiency compared with that of a single-color pulse. The high-energy and high peak-power water window IAP is expected to be significant for investigating single-shot imaging

in the soft X-ray region, studying life sciences, and performing attosecond-pump-attosecond-probe experiments to investigate the ultrafast dynamics of electrons, atoms, and molecules.

**Author Contributions:** Y.F. performed simulations of single atom using classical calculation and Lewestein model, and analysed data. P.L. developed the simulation code for calculation of HHG in gas cells. H.Y. and P.L. simulated HHs supercontinuum by the multi-cycle waveform synthesizer. K.M. directed the research. E.J.T. conceived the idea and supervised this project. Y.F., P.L., and E.J.T. discussed all the results and wrote the manuscript, which was polished by all of the authors.

**Funding:** This research was funded by JSPS KAKENHI (16K13704, 17H01067), and FY 2018 President's Discretionary Funds in RIKEN.

**Conflicts of Interest:** The authors declare no conflict of interest.

## References

1. Krausz, F.; Ivanov, M. Attosecond physics. *Rev. Mod. Phys.* **2009**, *81*, 163–234. [[CrossRef](#)]
2. Li, J.; Ren, X.; Yin, Y.; Zhao, K.; Chew, A.; Cheng, Y.; Cunningham, E.; Wang, Y.; Hu, S.; Wu, Y.; et al. 53-attosecond X-ray pulses reach the carbon K-edge. *Nat. Commun.* **2017**, *8*, 186. [[CrossRef](#)] [[PubMed](#)]
3. Gaumnitz, T.; Jain, A.; Pertot, Y.; Huppert, M.; Jordan, I.; Aardana-Lamas, F.; Jakob Wörner, H. Streaking of 43-attosecond soft-X-ray pulses generated by a passively CEP-stable mid-infrared driver. *Opt. Express* **2017**, *25*, 27506–27518. [[CrossRef](#)] [[PubMed](#)]
4. Goulielmakis, E.; Loh, Z.-H.; Wirth, A.; Santra, R.; Rohringer, N.; Yakovlev, V.S.; Zherebtsov, S.; Pfeifer, T.; Azzeer, A.M.; Kling, M.F.; et al. Real-time observation of valence electron motion. *Nature* **2010**, *466*, 739–743. [[CrossRef](#)] [[PubMed](#)]
5. He, L.; Zhang, Q.; Lan, P.; Cao, W.; Zhu, X.; Zhai, C.; Wang, F.; Shi, W.; Li, M.; Bian, X.; et al. Monitoring ultrafast vibrational dynamics of isotopic molecules with frequency modulation of high-order harmonics. *Nat. Commun.* **2018**, *9*, 1108. [[CrossRef](#)] [[PubMed](#)]
6. He, L.; Lan, P.; Le, A.T.; Wang, B.; Wang, B.; Zhu, X.; Lu, P.; Lin, C.D. Real-time observation of molecular spinning with angular high-harmonic spectroscopy. *Phys. Rev. Lett.* **2018**, *121*, 163201. [[CrossRef](#)]
7. Sommer, A.; Bothschafter, E.M.; Sato, S.A.; Jakubeit, C.; Latka, T.; Razskazovskaya, O.; Fattahi, H.; Jobst, M.; Schweinberger, W.; Shirvanyan, V.; et al. Attosecond nonlinear polarization and light-matter energy transfer in solids. *Nature* **2016**, *534*, 86–90. [[CrossRef](#)] [[PubMed](#)]
8. Hentschel, M.; Kienberger, R.; Spielmann, C.; Reider, G.A.; Milosevic, N.; Brabec, T.; Corkum, P.; Heinzmann, U.; Drescher, M.; Krausz, F. Attosecond metrology. *Nature* **2001**, *414*, 509–513. [[CrossRef](#)] [[PubMed](#)]
9. Heyl, C.M.; Arnold, C.L.; Couairon, A.; L'Huillier, A. Introduction to macroscopic power scaling principles for high-order harmonic generation. *J. Phys. B At. Mol. Opt. Phys.* **2017**, *50*, 013001. [[CrossRef](#)]
10. Spielmann, C.; Burnett, N.H.; Sartania, S.; Koppitsch, R.; Schnürer, M.; Kan, C.; Lenzner, M.; Wobrauschek, P.; Krausz, F. Generation of Coherent X-rays in the Water Window Using 5-Femtosecond Laser Pulses. *Science* **1997**, *278*, 661–664. [[CrossRef](#)]
11. Seres, C.; Seres, J.; Krausz, F.; Spielmann, C. Generation of Coherent Soft-X-ray Radiation Extending Far beyond the Titanium L Edge. *Phys. Rev. Lett.* **2004**, *92*, 163002. [[CrossRef](#)] [[PubMed](#)]
12. Ishii, N.; Kaneshima, K.; Kitano, K.; Kanai, T.; Watanabe, S.; Itatani, J. Sub-two-cycle, Carrier-envelope phase-dependent high harmonic generation in the water window using few-cycle infrared pulses. *Nat. Commun.* **2014**, *5*, 3331. [[CrossRef](#)] [[PubMed](#)]
13. Silva, F.; Teichmann, S.M.; Cousin, S.L.; Hemmer, M.; Biegert, J. Spatiotemporal isolation of attosecond soft X-ray pulses in the water window. *Nat. Commun.* **2015**, *6*, 6611. [[CrossRef](#)]
14. Takahashi, E.J.; Kanai, T.; Ishikawa, K.L.; Nabekawa, Y.; Midorikawa, K. Coherent water window x ray by phase-matched high-order harmonic generation in neutral media. *Phys. Rev. Lett.* **2008**, *101*, 253901. [[CrossRef](#)] [[PubMed](#)]
15. Takahashi, E.J.; Kanai, T.; Midorikawa, K. High-order harmonic generation by an ultrafast infrared pulse—Efficient generation of a coherent water window X-ray. *Appl. Phys. B* **2010**, *100*, 29–41. [[CrossRef](#)]
16. Brizuela, F.; Heyl, C.M.; Rudawski, P.; Kroon, D.; Rading, L.; Dahlström, J.M.; Mauritsson, J.; Johnsson, P.; Arnold, C.L.; L'Huillier, A. Efficient high-order harmonic generation boosted by below-threshold harmonics. *Sci. Rep.* **2013**, *3*, 1410. [[CrossRef](#)] [[PubMed](#)]

17. Seres, J.; Yakovlev, V.S.; Seres, E.; Strelci, C.; Wobrauschek, P.; Spielmann, C.; Krausz, F. Coherent superposition of laser-driven soft-X-ray harmonics from successive sources. *Nat. Phys.* **2007**, *3*, 878–883. [[CrossRef](#)]
18. Serrat, C.; Roca, D.; Seres, J. Coherent amplification of attosecond light pulses in the water-window spectral region. *Opt. Express* **2015**, *23*, 4867–4872. [[CrossRef](#)]
19. Serrat, C.; Roca, D.; Budesca, J.M.; Seres, J.; Seres, E.; Aurand, B.; Hoffmann, A.; Namba, S.; Kuehl, T.; Spielmann, C. Avalanche of stimulated forward scattering in high harmonic generation. *Opt. Express* **2016**, *24*, 8028–8044. [[CrossRef](#)]
20. Bredtmann, T.; Chelkowski, S.; Bandrauk, A.D.; Ivanov, M. XUV lasing during strong-field-assisted transient absorption in molecules. *Phys. Rev. A* **2016**. [[CrossRef](#)]
21. Takahashi, E.; Nabekawa, Y.; Otsuka, T.; Obara, M.; Midorikawa, K. Generation of highly coherent submicrojoule soft x rays by high-order harmonics. *Phys. Rev. A* **2002**. [[CrossRef](#)]
22. Takahashi, E.; Tosa, V.; Nabekawa, Y.; Midorikawa, K. Experimental and theoretical analyses of a correlation between pump-pulse propagation and harmonic yield in a long-interaction medium. *Phys. Rev. A* **2003**, *68*, 023808. [[CrossRef](#)]
23. Doumy, G.; Wheeler, J.; Roedig, C.; Chirla, R.; Agostini, P.; DiMauro, L.F. Attosecond synchronization of high-order harmonics from midinfrared drivers. *Phys. Rev. Lett.* **2009**, *102*, 093002. [[CrossRef](#)]
24. Chang, Z.; Corkum, P.B.; Leone, S.R. Attosecond optics and technology: Progress to date and future prospects. *J. Opt. Soc. Am. B* **2016**, *33*, 1081–1097. [[CrossRef](#)]
25. Trallero-Herrero, C.; Kajumba, N.; Bandulet, H.-C.; Comtois, D.; Légaré, F.; Giguère, M.; Kieffer, J.-C.; Corkum, P.B.; Villeneuve, D.M. Wavelength Scaling of High Harmonic Generation Efficiency. *Phys. Rev. Lett.* **2009**, *103*, 073902. [[CrossRef](#)]
26. Cousin, S.L.; Palo, N.D.; Buades, B.; Teichmann, S.M.; Reduzzi, M.; Devetta, M.; Kheifets, A.; Sansone, G.; Biegert, J. Attosecond streaking in the water window: A new regime of attosecond pulse characterization. *Phys. Rev. X* **2017**, *7*, 041030. [[CrossRef](#)]
27. Schiessl, K.; Ishikawa, K.L.; Persson, E.; Burgdörfer, J. Quantum path interference in the wavelength dependence of high-harmonic generation. *Phys. Rev. Lett.* **2007**, *99*, 253903. [[CrossRef](#)] [[PubMed](#)]
28. Zhang, J.; Mak, K.F.; Nag, N.; Seidel, M.; Bauer, D. Dirk Sutter, Vladimir Pervak, Ferenc Krausz and Oleg Pronin, Multi-mW, few-cycle mid-infrared continuum spanning from 500 to 2250  $\text{cm}^{-1}$ . *Light Sci. Appl.* **2017**. [[CrossRef](#)]
29. Kaneshima, K.; Ishii, N.; Takeuchi, K.; Itatani, J. Generation of carrier-envelope phase-stable mid-infrared pulses via dual-wavelength optical parametric amplification. *Opt. Express* **2016**, *24*, 8660–8665. [[CrossRef](#)] [[PubMed](#)]
30. Sanchez, D.; Hemmer, M.; Baudisch, M.; Cousin, S.L.; Zawilski, K.; Schunemann, P.; Chalus, O.; Simon-boisson, C.; Biegert, J. 7  $\mu\text{m}$ , ultrafast, sub-millijoule-level mid-infrared optical parametric chirped pulse amplifier pumped at 2  $\mu\text{m}$ . *Optica* **2016**, *3*, 147–150. [[CrossRef](#)]
31. Henke, B.L.; Gullikson, E.M.; Davis, J.C. X-ray interactions: Photoabsorption, scattering, transmission and reflection  $E = 50\text{--}30,000$  eV,  $Z = 1\text{--}92$ . *At. Data Nucl. Data Tables* **1993**, *54*, 181–342. [[CrossRef](#)]
32. Jin, C.; Wang, G.; Wei, H.; Le, A.-T.; Lin, C.D.; Waveforms for optimal sub-keV high-order harmonics with synthesized two- or three-colour laser fields. *Nat. Commun.* **2014**, *5*, 4003. [[CrossRef](#)]
33. Takahashi, E.J.; Lan, P.; Mücke, O.D.; Nabekawa, Y.; Midorikawa, K. Infrared two-color multicycle laser field synthesis for generating an intense attosecond pulse. *Phys. Rev. Lett.* **2010**, *104*, 233901. [[CrossRef](#)]
34. Takahashi, E.J.; Lan, P.; Mücke, O.D.; Nabekawa, Y.; Midorikawa, K. Attosecond nonlinear optics using gigawatt-scale isolated attosecond pulses. *Nat. Commun.* **2013**, *4*, 2691. [[CrossRef](#)]
35. Lan, P.; Takahashi, E.J.; Midorikawa, K. Isolated-attosecond-pulse generation with infrared double optical gating. *Phys. Rev. A* **2011**, *83*, 063839. [[CrossRef](#)]
36. Takahashi, E.J.; Lan, P.; Mücke, O.D.; Nabekawa, Y.; Midorikawa, K. Nonlinear attosecond metrology by intense isolated attosecond pulses. *IEEE J. Sel. Top. Quantum Electron.* **2015**, *21*, 8800112. [[CrossRef](#)]
37. Krauss, G.; Lohss, S.; Hanke, T.; Sell, A.; Eggert, S. Rupert Huber and Alfred Leitenstorfer, Synthesis of a single cycle of light with compact erbium-doped fibre technology. *Nat. Photonics* **2009**, *4*, 33–36. [[CrossRef](#)]
38. Chia, S.-H.; Cirmi, G.; Fang, S.; Rossi, G.M.; Mücke, O.D.; Kärtner, F.X. Two-octave-spanning dispersion-controlled precision optics for sub-optical-cycle waveform synthesizers. *Optica* **2014**, *1*, 315–322. [[CrossRef](#)]

39. Huang, S.-W.; Cirmi, G.; Moses, J.; Hong, K.-H.; Bhardwaj, S.; Birge, J.R.; Chen, L.-J.; Li, E.; Eggleton, B.J.; Cerullo, G.; et al. High-energy pulse synthesis with sub-cycle waveform control for strong-field physics. *Nat. Photonics* **2011**, *5*, 475–479. [[CrossRef](#)]
40. Xue, B.; Takahashi, E.J.; Fu, Y.; Midorikawa, K. Intense attosecond soft X-ray pulse by a high-energy three-channel waveform synthesizer. *Opt. Soc. Am. Tech. Dig.* **2017**. [[CrossRef](#)]
41. Corkum, P.B. Plasma perspective on strong-field multiphoton ionization. *Phys. Rev. Lett.* **1993**, *71*, 1994–1997. [[CrossRef](#)] [[PubMed](#)]
42. Zheng, Y.; Zeng, Z.; Zou, P.; Zhang, L.; Li, X.; Liu, P.; Li, R.; Xu, Z. Dynamic chirp control and pulse compression for attosecond high-order harmonic emission. *Phys. Rev. Lett.* **2009**, *103*, 043904. [[CrossRef](#)] [[PubMed](#)]
43. Zeng, Z.; Zheng, Y.; Cheng, Y.; Li, R.; Xu, Z. Attosecond pulse generation driven by a synthesized laser field with two pulses of controlled related phase. *J. Phys. B At. Mol. Opt. Phys.* **2012**, *45*, 074004. [[CrossRef](#)]
44. Kohler, M.C.; Keitel, C.H.; Hatsagortsyan, K.Z. Attochirp-free high-order harmonic generation. *Opt. Express* **2011**, *19*, 4411–4420. [[CrossRef](#)] [[PubMed](#)]
45. Lewenstein, M.; Balcou, P.; Ivanov, M.Y.; L’Huillier, A.; Corkum, P.B. Theory of high-harmonic generation by low-frequency laser fields. *Phys. Rev. A* **1994**, *49*, 2117–2131. [[CrossRef](#)] [[PubMed](#)]
46. Balcou, P.; Salières, P.; L’Huillier, A.; Lewenstein, M. Generalized phase-matching conditions for high harmonics: The role of field-gradient forces. *Phys. Rev. A* **1997**, *55*, 3204–3210. [[CrossRef](#)]
47. Ammosov, M.V.; Delone, N.B.; Krainov, V.P. Tunnel ionization of complex atoms and of atomic ions in an alternating electromagnetic field. *Sov. Phys. JETP* **1986**, *64*, 1191–1194. [[CrossRef](#)]
48. Priori, E.; Cerullo, G.; Nisoli, M.; Stagira, S.; Silvestri, S.D.; Villoresi, P.; Poletto, L.; Ceccherini, P.; Altucci, C.; Bruzese, R.; et al. Nonadiabatic three-dimensional model of high-order harmonic generation in the few-optical-cycle regime. *Phys. Rev. A* **2000**, *61*, 063801. [[CrossRef](#)]
49. Lan, P.; Lu, P.; Li, Q.; Li, F.; Hong, W.; Zhang, Q. Macroscopic effects for quantum control of broadband isolated attosecond pulse generation with a two-color field. *Phys. Rev. A* **2009**, *79*, 043413. [[CrossRef](#)]
50. Xiong, H.; Xu, H.; Fu, Y.; Yao, J.; Zeng, B.; Chu, W.; Cheng, Y.; Xu, Z.; Takahashi, E.J.; Midorikawa, K.; et al. Generation of a coherent x ray in the water window region at 1 kHz repetition rate using a mid-infrared pump source. *Opt. Lett.* **2009**, *34*, 1747–1749. [[CrossRef](#)]
51. Stein, G.J.; Keathley, P.D.; Krogen, P.; Liang, H.; Siqueira, J.P.; Chang, C.-L.; Lai, C.-J.; Hong, K.-H.; Laurent G.M.; Kärtner, F.X. Water-window soft X-ray high-harmonic generation up to the nitrogen K-edge driven by a kHz, 2.1  $\mu\text{m}$  OPCPA source. *J. Phys. B At. Mol. Opt. Phys.* **2016**, *49*, 155601. [[CrossRef](#)]
52. Fu, Y.; Midorikawa, K.; Takahashi, E.J. Towards a petawatt-class fewcycle infrared laser system via dual-chirped optical parametric amplification. *Sci. Rep.* **2018**, *8*, 7692. [[CrossRef](#)]
53. Zhang, Q.; Takahashi, E.J.; Mücke, O.D.; Lu, P.; Midorikawa, K. Dual-chirped optical parametric amplification for generating few hundred mJ infrared pulses. *Opt. Express* **2011**, *9*, 7190–7212. [[CrossRef](#)] [[PubMed](#)]
54. Fu, Y.; Takahashi, E.J.; Midorikawa, K. High-energy infrared femtosecond pulses generated by dual-chirped optical parametric amplification. *Opt. Lett.* **2015**, *40*, 5082–5085. [[CrossRef](#)] [[PubMed](#)]
55. Fu, Y.; Takahashi, E.J.; Zhang, Q.; Lu, P.; Midorikawa, K. Optimization and characterization of dual-chirped optical parametric amplification. *J. Opt.* **2015**, *17*, 124001. [[CrossRef](#)]
56. Fu, Y.; Takahashi, E.J.; Midorikawa, K. Energy Scaling of Infrared Femtosecond Pulses by Dual-Chirped Optical Parametric Amplification. *IEEE Photonics J.* **2017**, *9*, 1503108. [[CrossRef](#)]
57. Fu, Y.; Xue, B.; Midorikawa, K.; Takahashi, E.J. TW-scale mid-infrared pulses near 3.3  $\mu\text{m}$  directly generated by dual-chirped optical parametric amplification. *Appl. Phys. Lett.* **2018**, *112*, 241105. [[CrossRef](#)]
58. Takahashi, E.J.; Fu, Y.; Midorikawa, K. Carrier-envelope phase stabilization of a 16 TW, 10 Hz Ti:sapphire laser. *Opt. Lett.* **2015**, *40*, 4835–4838. [[CrossRef](#)]
59. Ishii, N.; Kaneshima, K.; Kitano, K.; Kanai, T.; Watanabe, S.; Itatani, J. Sub-two-cycle, carrier-envelope phase-stable, intense optical pulses at 1.6  $\mu\text{m}$  from a  $\text{BiB}_3\text{O}_6$  optical parametric chirped-pulse amplifier. *Opt. Lett.* **2012**, *37*, 4182–4184. [[CrossRef](#)]
60. Yin, Y.; Li, J.; Ren, X.; Zhao, K.; Wu, Y.; Cunningham, E.; Chang, Z. High-efficiency optical parametric chirped-pulse amplifier in  $\text{BiB}_3\text{O}_6$  for generation of 3 mJ, two-cycle, carrier-envelope-phase-stable pulses at 1.7  $\mu\text{m}$ . *Opt. Lett.* **2016**, *41*, 1142–1145. [[CrossRef](#)]

61. Mücke, O.D.; Fang, S.; Cirimi, G.; Rossi, G.M.; Chia, S.-H.; Ye, H.; Yang, Y.; Mainz, R.; Manzoni, C.; Farinello, P.; et al. Toward Waveform Nonlinear Optics Using Multimillijoule Sub-Cycle Waveform Synthesizers. *IEEE J. Sel. Top. Quantum Electron.* **2015**, *21*, 8700712. [[CrossRef](#)]
62. Mainz, R.; Rossi, G.M.; Cirimi, G.; Yang, Y.; Mücke, O.D.; Kärtner, F.X. High-dynamic-range arrival time control for flexible, accurate and precise parametric sub-cycle waveform synthesis. *Opt. Express* **2017**, *25*, 3052–3068. [[CrossRef](#)] [[PubMed](#)]
63. Fu, Y.; Takahashi, E.J.; Midorikawa, K. Indirect high-bandwidth stabilization of carrier envelope phase of a high-energy, low-repetition rate laser. *Opt. Express* **2016**, *24*, 13276–13287. [[CrossRef](#)] [[PubMed](#)]



© 2018 by the authors. Licensee MDPI, Basel, Switzerland. This article is an open access article distributed under the terms and conditions of the Creative Commons Attribution (CC BY) license (<http://creativecommons.org/licenses/by/4.0/>).